A Concentric Tube Continuum Robot with Piezoelectric Actuation for MRI-Guided Closed-Loop Targeting

Hao Su[1], **Gang Li**[2], **D. Caleb Rucker**[3], **Robert J. Webster III**[4], and **Gregory S. Fischer**[2]

[1]Wyss Institute for Biologically Inspired Engineering and the John A. Paulson School of Engineering and Applied Sciences, Harvard University, Cambridge, MA 02138, USA

[2]Automation and Interventional Medicine (AIM) Robotics Laboratory, Department of Mechanical Engineering, Worcester Polytechnic Institute, Worcester, MA 01609, USA

[3]Vanderbilt Institute in Surgery and Engineering, Vanderbilt University, Nashville, TN 37235, USA

[4]University of Tennessee, Knoxville, TN 37996, USA

Abstract

This paper presents the design, modeling and experimental evaluation of a magnetic resonance imaging (MRI)-compatible concentric tube continuum robotic system. This system enables MRI-guided deployment of a precurved and steerable concentric tube continuum mechanism, and is suitable for clinical applications where a curved trajectory is needed. This compact 6 degree-of-freedom (DOF) robotic system is piezoelectrically-actuated, and allows simultaneous robot motion and imaging with no visually observable image artifact. The targeting accuracy is evaluated with optical tracking system and gelatin phantom under live MRI-guidance with Root Mean Square (RMS) errors of 1.94 and 2.17 mm respectively. Furthermore, we demonstrate that the robot has kinematic redundancy to reach the same target through different paths. This was evaluated in both free space and MRI-guided gelatin phantom trails, with RMS errors of 0.48 and 0.59 mm respectively. As the first of its kind, MRI-guided targeted concentric tube needle placements with *ex vivo* porcine liver are demonstrated with 4.64 mm RMS error through closed-loop control of the piezoelectrically-actuated robot.

Keywords

MR-conditional; Concentric tube continuum robot; Image-guided surgery

INTRODUCTION

Image-guided surgery (IGS) enables high precision and improved outcomes for interventional procedures. However, typically only static preoperative images are available for intra-operative guidance, which are unable to provide updated and interactive information during a surgical procedure. MRI is an ideal guidance tool for IGS due to its ability to perform "real-time", high quality, volumetric imaging. The ability to redirect the

Address correspondence to: Hao Su, Wyss Institute for Biologically Inspired Engineering and the John A. Paulson School of Engineering and Applied Sciences, Harvard University, Cambridge, MA 02138, USA. haosu.ieee@gmail.com and gfischer@wpi.edu.

path of a needle once it has entered the body enables minimally invasive access to challenging surgical sites, as well as the ability to compensate for intra-operative tissue motion. A number of different approaches have been investigated to steer flexible needles,[2] including: (1) needle base manipulation of symmetric-tip needles,[9] (2) asymmetric tip-based needle steering,[28] (3) pre-curved tip needles,[16] and (4) concentric tube continuum robots (also referred to as active cannulas).[6,8,27,30] MRI-guided robotic surgery systems have been investigated with considerable efforts for neurosurgery,[25,10,14] prostate biopsy[31] and brachytherapy,[18] breast biopsy[11] and cardiac interventions.[26] However, the MRI compatibility issue, namely the mutual interference between the MR scanner and robotic system, is still a challenge.

From the actuation perspective, pneumatics and piezoelectrics are two of the most commonly used actuation methods. Stoianovici *et al.*[18] designed pneumatic stepper motors and applied them to the automatic brachytherapy seeds placement. Chen *et al.*[3] proposed a novel pneumatic stepper motor based on crank-link mechanism. Yang *et al.*[33] also investigated pneumatic motors for biopsy diagnosis of breast cancer.

Pneumatic actuation has the two key limitations for MRI-guided interventions. (1) Position control limitation: precise position control of servo-controlled pneumatic cylinders are difficult as nonlinear friction force and long pneumatic transmission lines may result in overshoot and instability. As observed in Yang *et al.*,[32] the oscillation amplitude is around 5 mm during a 25 mm step response (20% error) which would be unacceptable for a needle insertion procedure. One of the most advanced pneumatic stepping motors as described in Stoianovici *et al.*[22] overcomes the stability and overshoot issue, but is limited to a 3.3° step angle. In contrast, the step angle of the rotary piezoelectric motor in our robot (PiezoLegs, LR80, PiezoMotor AB, Sweden) is 5.73×10^{-6} degree. (2) Bulky size limitation: the aforementioned piezoelectric rotary motor has a 23 mm diameter by 34.7 mm length, as compared with the pneumatic stepper motor's $70 \times 20 \times 25$ mm dimensions.

However, without careful design considerations imaging noise during simultaneous imaging and motion is evident. This is clearly visible with commercially available piezoelectric motor drivers.[7] Krieger *et al.*[12] reported that piezoelectric motors utilizing commercially available motor drivers cause unacceptable MR imaging noise (up to 40 – 80% signal loss) during simultaneous imaging and robot motion. This is the technical hurdle overcome by the custom piezoelectric motor controller utilizing a direct digital synthesizer waveform generator and specially designed amplification circuit in this paper.

This manuscript describes the design and evaluation of an MRI-guided concentric tube continuum robotic system, combining our recently developed framework for MR-conditional piezoelectric actuation[23] with a concentric tube robot deployed as a steerable needle. We describe a new robot system and the first-ever closed loop-targeting results with a concentric tube robot in an MRI scanner. These experiments are also the first conducted in biological tissues with concentric tube robots in an MRI scanner, while all prior studies have used phantoms. Some results in this manuscript appeared in preliminary conference paper form in Su *et al.*[24] Notable additions and extensions include that the current experiments are closed loop (i.e., using targets identified directly on MRI images) rather than open loop (i.e.,

deployment without specific image-frame targets). This is the first archival publication on the use of concentric tube robots in the MRI scanner with a piezoelectrically-actuated robotic system.

MATERIALS AND METHODS

Kinematics Model

Our prototype concentric tube robot is made of three concentric elastic tubes. The outer tube and inner tube are naturally straight, while the middle tube has a pre-curved section at its tip with a constant curvature $\kappa = 0.0138$/mm. This parameter was determined by preliminary estimation for Ultrasonic Interstitial Thermal Therapy (USITT)[4] liver ablation application. Further tube geometry optimization is required for the specific clinical intervention based on anatomy and constraints, following the method proposed be Bergeles *et al.*[1] The results presented for this example configuration may be generalized to other configurations based on tube geometry optimization.

The inner elastic tube is solid wire, which in our clinical application represents a USITT ablator[4] but could also represent another diagnostic or therapy delivery instrument. Nickel titanium, also known as nitinol, is used to fabricate the tubes and wire, due to its unique characteristics of sustaining high strain without damage (sustain recoverable strain of as much as $\varepsilon = 11\%$),[5] and high torsional rigidly compared to their flexural rigidity.

In general, torsional effects are important to consider whenever there are two or more tubes with overlapping curved sections. General model with no external loads has been studied by Dupont *et al.*[6] and Rucker *et al.*[19] General model with external loads was presented by Rucker *et al.*[20] and Lock *et al.*[15] The particular design in this paper eliminates the need to consider torsion because there is only one pre-curved tube and hence no torsional deformation except that which is due to friction. So the model presented in this section is a special case where the general model reduces to a simple algebraic model due to the design choice of having only one precurved tube. However, the model in this paper (and our recent conference papers[24 and 13]) is the only one to consider the angular offset resulting from tube clearances, which has been a source of error in prior models. The model was established under the main assumption of linear elasticity (constant Young's modulus) and the dominance of bending effects over the shear effects induced by bending.

Mechanics of Concentric Tubes

An interaction effect occurs among the precurved tubes, which are placed concentrically, causing bending into a combined shape different from the natural at-rest geometry of individual tubes. To describe the complete shape of the concentric tube robot, a mechanics model is established for the shape of a single "link" composed of several overlapping concentric curved tubes, based on the Bernoulli-Euler beam equation[29]:

$$\Delta\kappa = \frac{M}{EI} \quad (1)$$

where $\Delta\kappa = \kappa - \kappa_i$ is the difference between the deformed curvature, κ, and the "at rest" precurvature, κ_i. M is the internal moment carried by the tube, E is the modulus of elasticity (Young's modulus), and I is the cross-sectional moment of inertia. In a similar way of describing the equilibrium position of linear springs of different lengths and stiffness when connected in parallel by a force balance, the resultant curvature in a segment of n overlapping tubes whose natural planes of curvature are aligned by:

$$k_r = \frac{\sum_{i=1}^{n} E_i I_i k_i}{\sum_{i=1}^{n} E_i I_i} \quad (2)$$

for n tubes, where k_i are the preformed curvatures of the individual tubes.

Forward Kinematics

Forward kinematics of a concentric tube robot is a description of complete device shape in terms of the joint variables. The prototype concentric tube robot consists of four segments, each with constant curvature as shown in Fig. 1. The length of each segment l_1, l_2, l_3, l_4 are calculated from the actuated distances q_1, q_2, q_3, which are the insertion distance of each tube's tip from its starting point. The starting point (i.e., home position) is defined to be the position where tips of each tube are at the constrained entry point. Considering the finite clearance between tubes, there would be an angular offset of a between the middle and outer tube, and an angular offset of λ between the middle and inner tube. The offset angles were experimentally measured using graph paper, then calibrated by fitting the kinematic model.

The initial values of offset angles ($a = 15°$, $\lambda = -2°$) are obtained by measuring the angle of 2 tangent lines at each segment, and then calibrated by fitting the theoretical model with experiment data to get the offset values which have minimum fitting errors The constant tube length parameters are $L_1 = 65$ mm, $L_2 = 162$ mm, $L_c = 74$ mm, and $L_3 = 340$ mm.

The lengths of the sections shown in Fig. 1 are given by:

$$l_1 = max(q_2 - L_c, 0) \quad (3)$$

$$l_2 = max(q_1 - l_1, 0) \quad (4)$$

$$l_3 = max(q_2 - l_2 - l_1, 0) \quad (5)$$

$$l_4 = max(q_3 - l_3 - l_2 - l_1, 0) \quad (6)$$

L_c is the length of the pre-curved section of the middle tube (tube 2). The curvatures of overlapping sections k_{123} and k_{23} are:

$$k_{123} = \frac{E_2 I_2 k_2}{E_1 I_1 + E_2 I_2 + E_3 I_3} \quad (7)$$

$$k_{23} = \frac{E_2 I_2 k_2}{E_2 I_2 + E_3 I_3} \quad (8)$$

where E_i is the Young's Modulus of the ith tube (i.e., i = 1, 2, 3, corresponding to outer, middle and inner tubes respectively) and I_i is the cross sectional moment of inertia of the tube. Forward kinematics consists of the series of homogeneous transformations, where the tip coordinate frame is determined with respect to a base frame located at the constrained entry point by:

$$T_{tip} = T_1 T_\theta T_2 T_\alpha T_3 T_\lambda T_4 \quad (9)$$

where intermediate transformations are defined as:

$$T_1 = \begin{bmatrix} 1 & 0 & 0 & 0 \\ 0 & 1 & 0 & 0 \\ 0 & 0 & 1 & l_1 \\ 0 & 0 & 0 & 1 \end{bmatrix}$$

$$T_\theta = \begin{bmatrix} \cos\theta & -\sin\theta & 0 & 0 \\ \sin\theta & \cos\theta & 0 & 0 \\ 0 & 0 & 1 & 0 \\ 0 & 0 & 0 & 1 \end{bmatrix}$$

$$T_2 = \begin{bmatrix} 1 & 0 & 0 & 0 \\ 0 & \cos(k_{23}l_2) & -\sin(k_{23}l_2) & \frac{\cos(k_{23}l_2)-1}{k_{23}} \\ 0 & \sin(k_{23}l_2) & \cos(k_{23}l_2) & \frac{\sin(k_{23}l_2)}{k_{23}} \\ 0 & 0 & 0 & 1 \end{bmatrix}$$

$$T_\alpha = \begin{bmatrix} 1 & 0 & 0 & 0 \\ 0 & \cos\alpha & -\sin\alpha & 0 \\ 0 & \sin\alpha & \cos\alpha & 0 \\ 0 & 0 & 0 & 1 \end{bmatrix}$$

$$T_3 = \begin{bmatrix} 1 & 0 & 0 & 0 \\ 0 & \cos(k_{123}l_3) & -\sin(k_{123}l_3) & \frac{\cos(k_{123}l_3)-1}{k_{123}} \\ 0 & \sin(k_{123}l_3) & \cos(k_{123}l_3) & \frac{\sin(k_{123}l_3)}{k_{123}} \\ 0 & 0 & 0 & 1 \end{bmatrix}$$

$$T_\lambda = \begin{bmatrix} 1 & 0 & 0 & 0 \\ 0 & \cos\lambda & -\sin\lambda & 0 \\ 0 & \sin\lambda & \cos\lambda & 0 \\ 0 & 0 & 0 & 1 \end{bmatrix}$$

$$T_4 = \begin{bmatrix} 1 & 0 & 0 & 0 \\ 0 & 1 & 0 & 0 \\ 0 & 0 & 1 & l_4 \\ 0 & 0 & 0 & 1 \end{bmatrix}$$

(10)

Thus, T_{tip} gives the 6-DOF position and orientation of the tip of the concentric tube robot as a function of the measured actuator configurations: q_1, q_2, q_3 and θ.

Inverse Kinematics for Closed-loop Control

To place the tip of the concentric tube robot at a desired target with specific joint configuration, the forward kinematic mapping given must be inverted. To this end, we perform a nonlinear optimization based on the Levenberg–Marquardt algorithm. This enables us to resolve the joint values which minimize the errors between the predicted kinematic model and desired tip position. The predicted tip position are resolved by a uniform 100×100 joint space discretization (middle tube translation ×Prior evaluation in inner wire translation, i.e., $q_2 \times q_3$), and then computing the predicted tip position at each configuration using the forward kinematics model. Based on the configuration of the robot, the outer tube translation q_1 is a constant value in this study, and middle tube rotation can be calculated geometrically, i.e., $\theta = atan2(x, y)$, where x and y are the elements of needle tip Cartesian position vector. At each configuration, the nonlinear optimization function lsqnonlin in Matlab is utilized to resolve the joint values (overall computation time within 250 ms for 100×100 joint space calculation) that minimizes the errors between the

predicted and desired tip position, as well as the residual errors, with predicted joint values as the initial guess of the lsqnonlin function. The final solutions of joint values are obtained by choosing the configuration which is the interpolation of multiple closest residual errors among all the configurations.

ROBOTIC SYSTEM DESIGN

MR-Conditional Concentric Tube Manipulator

The robot mechanism is designed to perform needle-based interventional procedures. In this study, it is configured to perform precise control of the three concentric tubes forming the concentric tube robot upon a base platform. The 6-DOF robot consists of two kinematically-decoupled modules, namely the 3-DOF Cartesian base stage and the 3-DOF needle driver module, as shown in Fig. 2. The Cartesian stage provides 3-DOF motion for placement of the constrained entry point of concentric tube robot. The needle driver module provides 1-DOF translation (q_2) and 1-DOF rotation (θ) of the precurved middle tube, and 1-DOF translation (q_3) of the inner wire. The Cartesian stage positions the tip of the outer-most tube, while the needle driver module grasps the pre-curved middle tube with a collet to control its rotation and translation and clamps the proximal end of the inner wire to translate within the middle tube. Additional detail about the manipulator upon which this system was adapted is described in Su *et al.*[23]

Piezoelectric Actuation System

Prior evaluation in MRI demonstrated significant degradation of image quality with signal noise ratio (SNR) reduction of up to 40–80%.[12] To address this issue, a custom piezoelectric motor controller was developed. In our implementation, the driving signal is generated from direct digital synthesizer (DDS), and passes through four linear amplifiers and π filters out to the piezoelectric actuator. The amplifiers produce 4-channels of clean driving signals for the four quasistatic legs (A, B, C, and D legs) forming a stator which interchangeably establish frictional contact to a ceramic drive preloaded with a beryllium copper leaf spring. Further electrical design details have been described in Su *et al.*[23]

Image-Based Registration and Control

To register the robot to the patient coordinate system in the image space—referred to as Right-Anterior-Superior (RAS) coordinates—a fiducial frame is firmly attached to the base of the robot as shown in Fig. 3. The fiducial frame is composed of seven tubes filled with MR-visible, high contrast fluid (Beekley, Bristol, CT), and configured in a set of Z shapes in each of the three orthogonal planes, as shown in Fig. 4 (left). Figure 4 (right) illustrates one T2-weighted fast spin echo image of the tracking fiducial frame.[21]

The corresponding serial chain of homogeneous transformations was used to determine the tip location in the RAS coordinates is:

$$T_{Tip}^{RAS} = T_Z^{RAS} T_{Base}^Z T_{Rob}^{Base} T_{Tip}^{Rob} \quad (11)$$

where T^{RAS}_{Tip} is the desired needle tip in the RAS coordinate system, T^{RAS}_Z is fiducial's 6-DOF coordinates with respect to RAS as determined by the fiducial frame registration, T^Z_{Base} is the mechanically fixed location of the fiducial frame on the robot base as determined based on robot calibration, T^{Base}_{Rob} is the position of the constrained entry point of concentric tube robot with respect to the robot base which is determined from the kinematics of the 3-DOF Cartesian stage, and T^{Rob}_{Tip} in the tip position of concentric tube robot with respect to the constrained entry point as determined by the concentric tube robot kinematics defined in "Materials and Methods" section.

RESULTS

The performance of this robot, primarily the targeting accuracy in three different medium (free space, gelatin phantom and *ex vivo* tissue), has been studied and is reported in this section. A series of experiments were conducted to systematically demonstrate the capability and error sources of this robotic system.

Task Space Accuracy Assessment Utilizing Optical Tracking System

The accuracy of the robot in task space was evaluated using a Polaris (Northern Digital, Ontario, Canada) optical tracking system (OTS). The stated 3D volumetric accuracy of the Polaris is 0.35 mm, and based on our assessment the standard deviation of the readings for a given stable point is 0.10 mm. A 6-DOF passive tracking tool rigid body composed of a circular plate and 3 passive spheres was rigidly mounted on the base of the robot, serving as the global reference during this experiment, i.e., all the data are recorded with respect to this 6-DOF reference frame. One passive sphere is attached at the tip of inner wire of the concentric tube robot to serve as the tip tracking marker of OTS, as shown in Fig. 5.

The concentric tube robot is commanded to 12 targets (3 targets in each of 4 planes) that were specified as virtual points in the coordinate system of fiducial frame on the robot base. The actual tip position is measured by collecting 300 frames at 30 Hz using OTS, with respect to reference frame. The fiducial frame is registered to OTS reference frame *via* 3 feature points, i.e.,, the center point, and an arbitrary point in each of the *x* axis and the *z* axis of the fiducial frame. Based on these 3 featured points, the fiducial frame can be registered to the reference frame. The accuracy is evaluated by comparing the intended and actual tip position, both in the coordinate system of fiducial frame.

The results obtained from the benchtop evaluation are shown in Fig. 6, demonstrating RMS error of 1.94 mm and standard deviation of 0.97 mm for the 12 targets, validating the accuracy of the robotic system as well as the kinematics model.

MRI-Guided Closed-loop Multiple-Point Targeting with Gelatin Phantom

In light of the positioning capability of the robot in free space, the system was further evaluated with image-guided targeting based on desired pixels in the MR image volume. This study was performed in a gelatin phantom. Knox Gelatin (Kraft Foods Global Inc., IL) was mixed with boiling water at a concentration of 3% (by weight). The phantom was

placed on the bed of a 3 Tesla MRI scanner (Philips Achieva, Best, Netherlands) between 2 flex coils to enhance the imaging quality. The robot was placed beside the phantom, and the bed was adjusted to place the phantom at the isocenter of the scanner. The phantom was imaged with a diagnostic T2-weighted fast spin echo protocol (repetition time 800 ms, echo time 11 ms, slice thickness 1.0, 0.9 mm × 0.9 mm pixel size). The robot was commanded to 12 targets that were selected from the 3D MRI images and 70 images slices of the phantom were acquired for each trajectory to verify the trajectory (Fig. 7).

The results from 12 robotic active cannula closed-loop targeting overlaid with the theoretical model are shown in Fig. 8, which demonstrates an RMS error of 2.17 mm and standard deviation of 0.97 mm.

Demonstration of Available Redundancy with Phantom Trials in MRI

This concentric tube manipulator can achieve remote center of motion like movement to reach a given target point from various trajectories by utilizing different joint space configurations. With the active cannula, this could be potentially employed to avoid obstacles. To demonstrate this redundancy, a series of experiments were conducted in both free space and phantom trials.

Assessment in Free Space—This concept was qualitatively demonstrated based on camera recording and the accuracy in free space quantitatively evaluated by the OTS. An arbitrary target point was selected within the workspace of robot, and 3 solutions of trajectories with different joint configurations were solved based on the inverse kinematics. In these experiments, the rotation angle of middle tube was set to a constant value (90°), i.e., the 3 trajectories are in the same plane. It should be noted that this is intended as an example of the ability to reach a target point from multiple trajectories, and the set of reachable paths includes a full 360° rotation. The simulated 3 trajectories with a common tip position are shown in Fig. 9.

To qualitatively demonstrate the concept, a bench-top test was setup with a digital 10.1 mega-pixel CCD camera (Panasonic Lumix DMC-LX5, Japan) rigidly mounted on the top of robot, with lens axis perpendicular to the horizontal plane. A grid paper was used as a reference to localize the tip position. The robot was commanded to the given target point with 3 solved solutions, and their trajectories were recorded by the camera. The 3 trajectories were overlaid in the same figure shown in Fig. 10 to visually illustrate this kinematic redundancy.

For a quantitative analysis, using a similar procedure described in "Task Space Accuracy Assessment Utilizing Optical Tracking System" section, a spherical tracking marker was attached on the innermost tip of active cannula to record the actual tip position with respect to the 6-DOF reference frame. The robot was commanded to the 3 solved trajectories (the same target position from multiple approach paths), and then the accuracy was evaluated by comparing the theoretical and actual tip positions. The experiment demonstrated RMS error of 0.48 mm, and standard deviation of 0.16 mm.

Assessment with Phantom Trials in MRI—This dexterity that can reach the same target with different path due to position kinematic redundancy was evaluated with phantom trials under live MRI guidance. With the same experimental setup as described in "MRI-Guided Closed-loop Multiple-Point Targeting with Gelatin Phantom section, the active cannula was placed in the soft gelatin phantom to an arbitrary point with 3 different sets of joint configurations, imaged with T2-weighted protocol. Figure 11 shows slices from the 3D MR image volume of the 3 trajectories. The accuracy of tip positions was evaluated by comparing the theoretical (calculated based on the kinematic model) and actual tip positions (determined by the position of the corresponding signal void in each slice), which demonstrating RMS error of 0.59 mm, and standard deviation of 0.12 mm in reaching the same point from different paths.

MRI-Guided Closed-loop Multiple-Point Targeting Within Ex Vivo Tissue

An *ex vivo* liver tissue study was conducted as a demonstration under live MRI guidance. A fresh porcine liver, with approximated dimension of 200 mm × 150 mm × 50 mm was used as the specimen. The specimen was rigidly attached to the phantom frame, which was mounted on the robot base, to reduce the motion of specimen during insertion (Fig. 12).

Three targets were selected from the MRI volume, then the concentric tube robot calculated inverse kinematics to command the motors to generate the tube motion to desired reference point. The final path was imaged with T2-weighted fast spin echo protocol (repetition time 800 ms, echo time 11 ms, slice thickness 1.0, 0.9 × 0.9 mm pixel size) for accuracy evaluation. Figure 13 shows the MRI image volume for one of the curved trajectories. In this image, 70 axial slices (0.9 mm × 0.9 mm × 1.0 mm voxel size) composed into a 3D volume which is resliced into the three orthogonal planes shown. In each set of MRI images, the actual 3D trajectory of the inserted cannula is measured by determining the position of the corresponding signal void in each slice.

Figure 14 shows the three curved trajectories to reach targets in the *ex vivo* tissue and red spheres indicate the desired positions. For a quantitative evaluation, Table 1 shows the needle placement error in terms of the desired position in MRI and the manually segmented actual needle tip position. The Cartesian positioning errors of the three trajectories are: 3.79, 2.87, and 6.48 mm, respectively. Clinically, there is no consensus about the targeting accuracy standard depending on different organ interventions and treatment methods. But roughly, it is agreed that 1 cm or ideally 5 mm accuracy (e.g., 5 mm is the grid spacing of prostate biopsy guide template) is satisfactory.

DISCUSSION

The kinematic modeling and accuracy of the MRI-guided concentric tube continuum robot presented in this paper was evaluated thorough experiments. The targeting capability of the system in free space was accomplished with an RMS error of 1.96 mm. The closed-loop targeting capability of the system was further evaluated in soft gelatin phantom under live MRI guidance with an RMS error of 2.18 mm. Compared with the results in free space, small additional errors are introduced by the interaction force with the external medium (i.e., gelatin phantom) and the ability to detect needle artifact in MRI image. While for the *ex*

vivo tissue interventional procedures under the same MRI image sequence, the RMS error of 4.64 mm is mostly due to the interaction force with the external medium, i.e., porcine liver, which is relatively large compared to that of the soft gelatin phantom. This obviously imposes challenges in *in vivo* needle placement and targeting.

Our proposed image-guided closed-loop control method only utilizes MRI to define targets and evaluate targeting accuracy. To further utilize the imaging capability of MRI, one effort from our group is to dynamically scan, track and align imaging plane to visualize the needle trajectory for closed-loop control of needle tip motion.[17] We envision that the same imaging technique can be extended from a bevel-tip needle steering scenario[17] to the concentric tube robot applications. Future research will focus on preparation for neurosurgical interventions through cadaver and in-human-trials, as well as on improving accuracy of the kinematic model by integrating frictional force and compensating the interaction force with tissue.

Acknowledgments

References

1. Bergeles C, Gosline AH, Vasilyev NV, Codd PJ, del Nido PJ, Dupont PE. Concentric tube robot design and optimization based on task and anatomical constraints. IEEE Trans Robot. 2015; 31(1): 67–84. [PubMed: 26380575]

2. Bergeles C, Yang GZ. From passive tool holders to microsurgeons: safer, smaller, smarter surgical robots. IEEE Trans Biomed Eng. 2014; 61(5):1565–1576. [PubMed: 24723622]

3. Chen Y, Kwok KW, Tse ZTH. An MR-conditional high-torque pneumatic stepper motor for MRI-guided and robot-assisted intervention. Ann Biomed Eng. 2014; 42(9):1823–1833. [PubMed: 24957635]

4. Diederich C, Stafford R, Nau W, Burdette E, Price R, Hazle J. Transurethral ultrasound applicators with directional heating patterns for prostate thermal therapy: in vivo evaluation using magnetic resonance thermometry. Med Phys. 2004; 31:405. [PubMed: 15000627]

5. Duerig T, Pelton A, Stöckel D. An overview of nitinol medical applications. Mater Sci Eng A. 1999; 273:149–160.

6. Dupont P, Lock J, Itkowitz B, Butler E. Design and control of concentric-tube robots. IEEE Trans Robot. 2010; 26(2):209–225. [PubMed: 21258648]

7. Fischer GS, Krieger A, Iordachita I, Csoma C, Whitcomb LL, Fichtinger G. MRI compatibility of robot actuation techniques—a comparative study. International Conference on Medical Image Computing and Computer Assisted Intervention. 2008:509–517.

8. Gilbert H, Neimat J, Webster R. Concentric tube robots as steerable needles: achieving follow-the-leader deployment. IEEE Trans Robot. 2015; 31:246–258. [PubMed: 26622208]

9. Glozman D, Shoham M. Image-guided robotic flexible needle steering. IEEE Trans Robot. 2007; 23:459–467.

10. Ho M, McMillan A, Simard J, Gullapalli R, Desai J. Toward a SMA-actuated MRI-compatible neurosurgical robot. IEEE Trans Robot. 2012; 28:213–222.

11. Iranpanah B, Chen M, Patriciu A, Sirouspour S. A pneumatically actuated target stabilization device for MRI-guided breast biopsy. IEEE/ASME Trans Mechatron. 20:1288–1300.

12. Krieger A, Song S, Bongjoon Cho N, Iordachita I, Guion P, Fichtinger G, Whitcomb LL. Development and evaluation of an actuated MRI-compatible robotic system for MRI-guided prostate intervention. IEEE/ASME Trans Mechatron. 2012; (99):1–12.

13. Lathrop, R., Rucker, DC., Webster, RJ., III, et al. Guidance of a steerable cannula robot in soft tissue using preoperative imaging and conoscopic surface contour sensing. 2010 IEEE International Conference on Robotics and Automation (ICRA); IEEE; 2010. p. 5601-5606.

14. Li G, Su H, Cole G, Shang W, Harrington K, Camilo A, Pilitsis JG, Fischer GS. Robotic system for MRI-guided stereotactic neurosurgery. IEEE Trans Biomed Eng. 2015; 62(4):1077–1088. [PubMed: 25376035]

15. Lock, J., Laing, G., Mahvash, M., Dupont, PE. Quasistatic modeling of concentric tube robots with external loads. 2010 IEEE/RSJ International Conference on Intelligent Robots and Systems (IROS); IEEE; 2010. p. 2325-2332.

16. Okazawa S, Ebrahimi R, Chuang J, Salcudean SE, Rohling R. Hand-held steerable needle device. IEEE/ASME Trans Mechatron. 2005; 10(3):285–296.

17. Patel, NA., van Katwijk, T., Li, G., Moreira, P., Shang, W., Misra, S., Fischer, GS. Closed-loop asymmetric-tip needle steering under continuous intraoperative MRI guidance. Engineering in Medicine and Biology Society, EMBC, Annual International Conference of the IEEE; 2015. p. 6687-6690.

18. Patriciu A, Patriciu A, Petrisor D, Muntener M, Mazilu D, Schar M, Stoianovici D. Automatic brachytherapy seed placement under MRI guidance. IEEE Trans Biomed Eng. 2007; 54(8):1499–1506. [PubMed: 17694871]

19. Rucker DC, Webster RJ, Chirikjian GS, Cowan NJ. Equilibrium conformations of concentric-tube continuum robots. Int J Robot Res. 2010; 29(10):1263–1280.

20. Rucker D, Jones B, Webster RJ III. A geometrically exact model for externally loaded concentric-tube continuum robots. IEEE Trans Robot. 2010; 26:769–780. [PubMed: 21566688]

21. Shang, W., Fischer, GS. A high accuracy multi-image registration method for tracking MRI-guided robots. SPIE Medical Imaging (Image-Guided Procedures, Robotic Interventions, and Modeling Conference); San Diego, USA. 2012.

22. Stoianovici D, Stoianovici D, Patriciu A, Petrisor D, Mazilu D, Kavoussi L. A new type of motor: pneumatic step motor. IEEE/ASME Trans Mechatron. 2007; 12(1):98–106.

23. Su H, Shang W, Cole G, Li G, Harrington K, Camilo A, Tokuda J, Tempany CM, Hata N, Fischer GS. Piezoelectrically-actuated robotic system for MRI-guided prostate percutaneous therapy. IEEE/ASME Trans Mechatron. 2015; 99(3):1–13.

24. Su, H., Cardona, D., Shang, W., Camilo, A., Cole, G., Rucker, D., Webster, R., Fischer, G. MRI-guided concentric tube continuum robot with piezoelectric actuation: a feasibility study. IEEE International Conference on Robotics and Automation (ICRA); 2012. p. 1939-1945.

25. Sutherland GR, Latour I, Greer AD, Fielding T, Feil G, Newhook P. An image-guided magnetic resonance-compatible surgical robot. Neurosurgery. 2008; 62:286–292. discussion 292–3. [PubMed: 18382307]

26. Tsekos N, Khanicheh A, Christoforou E, Mavroidis C. Magnetic resonance-compatible robotic and mechatronics systems for image-guided interventions and rehabilitation: a review study. Annu Rev Biomed Eng. 2007; 9:351–387. [PubMed: 17439358]

27. Vandini, A., Bergeles, C., Lin, F-Y., Yang, G-Z. Vision-based intraoperative shape sensing of concentric tube robots. IEEE/RSJ International Conference on Intelligent Robots and Systems; 2015. p. 3505-3510.

28. Webster RJ III, Kim JS, Cowan N, Chirikjian G, Okamura A. Nonholonomic modeling of needle steering. Int J Robot Res. 2006; 25(5–6):509–525.

29. Webster RJ, Romano JM, Cowan NJ. Mechanics of precurved-tube continuum robots. IEEE Trans Robot. 2009; 25(1):67–78.

30. Wu, K., Wu, L., Ren, H. An image based targeting method to guide a tentacle-like curvilinear concentric tube robot. 2014 IEEE International Conference on Robotics and Biomimetics (ROBIO); IEEE; 2014.

31. Yakar D, Schouten MG, Bosboom DGH, Barentsz JO, Scheenen TWJ, Futterer JJ. Feasibility of a pneumatically actuated MR-compatible robot for transrectal prostate biopsy guidance. Radiology. 2011; 260(1):241–247. [PubMed: 21406625]

32. Yang B, Tan UX, McMillan AB, Gullapalli R, Desai JP. Design and control of a 1-DOF MRI-compatible pneumatically actuated robot with long transmission lines. IEEE/ASME Trans Mech. 2011; 16(6):1040–1048.

33. Yang B, Roys S, Tan UX, Philip M, Richard H, Gullapalli RP, Desai JP. Design, development, and evaluation of a master–slave surgical system for breast biopsy under continuous MRI. Int J Robot Res. 2013:616–630.
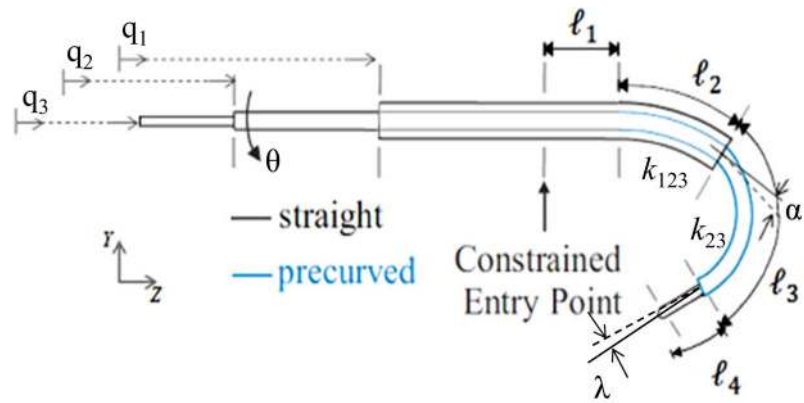
FIGURE 1.
Illustration of the 3-segment concentric tube continuum manipulator kinematics with the joint variables.
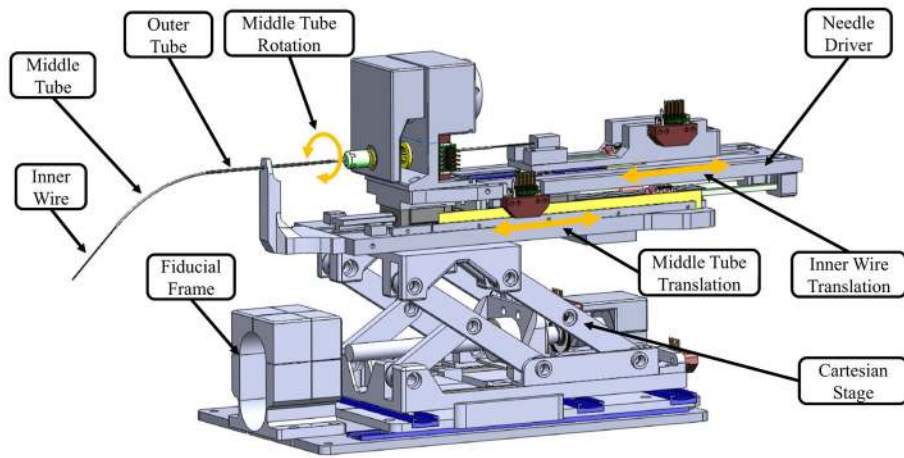
FIGURE 2.
3D CAD model of the concentric tube manipulator showing Cartesian base stage, needle driver module, fiducial frame, and the 3 concentric tubes.
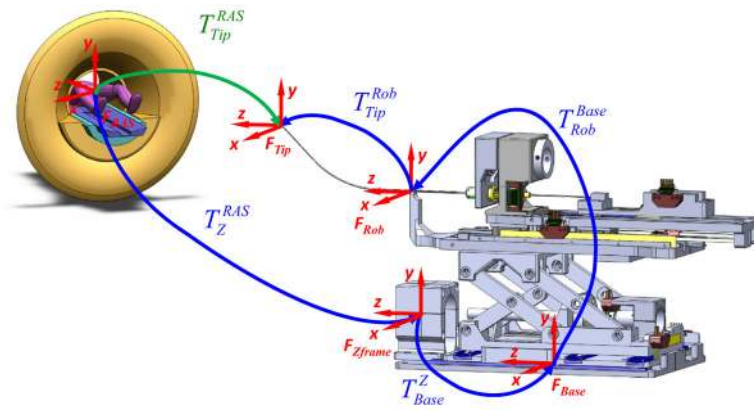
FIGURE 3.
The coordinate system and kinematic chain is used to determine the tip location in the RAS coordinates.
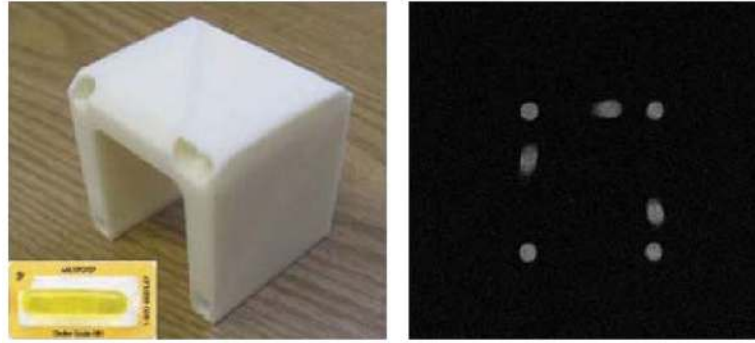
FIGURE 4.
The Z-frame registration fiducial (left) with corresponding cross-sectional MR image (right).

FIGURE 5.
The optical tracking system for validation of concentric tube robot kinematics and assessment of free space accuracy.
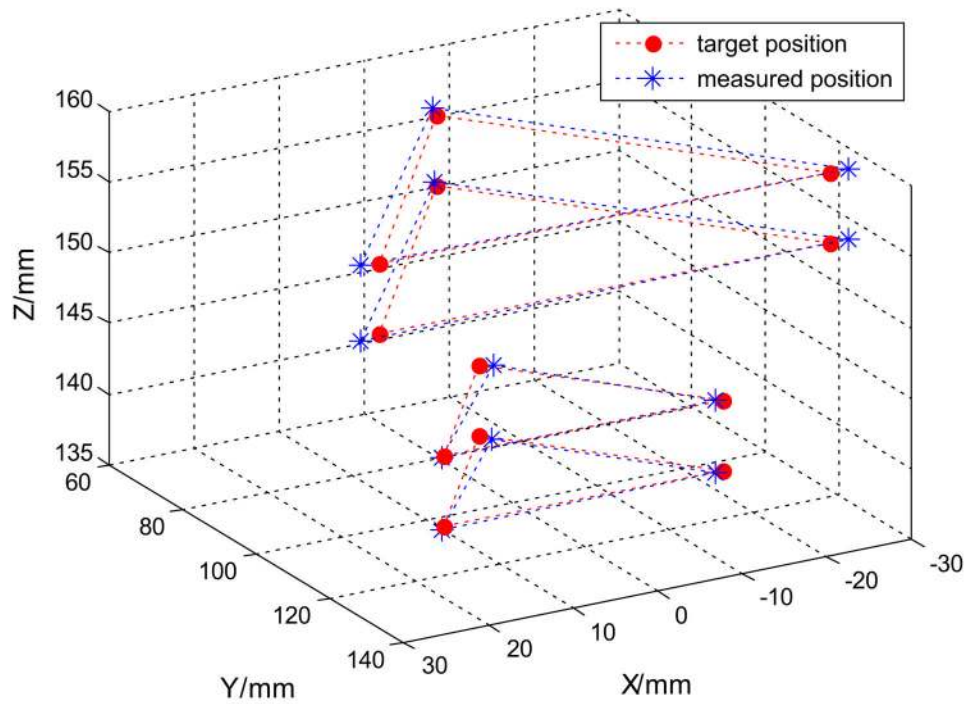
FIGURE 6.
Free space evaluation of the accuracy of the active cannula robot. The concentric tube robot was moved to 12 desired points (red circles) in free space and the actual position was measured by the optical tracker (blue stars).
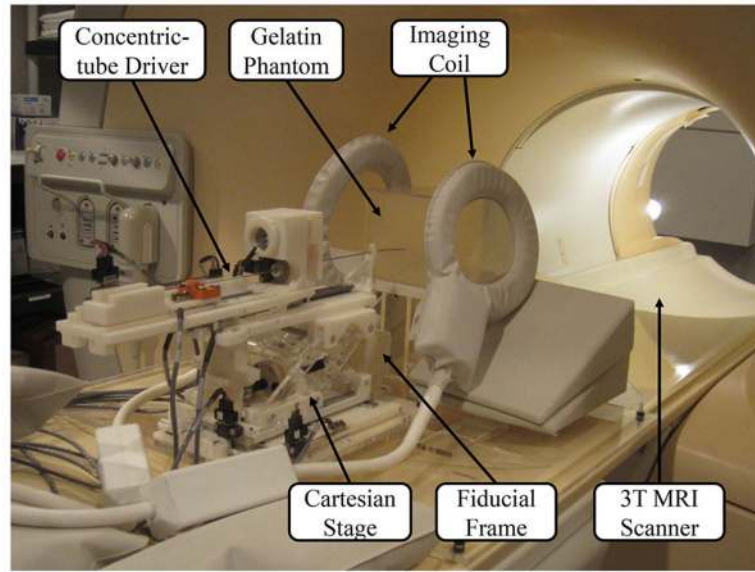
FIGURE 7.
The phantom and robot experimental setup illustrating the concentric tube continuum robot at the entrance of the 3T MRI scanner bore.
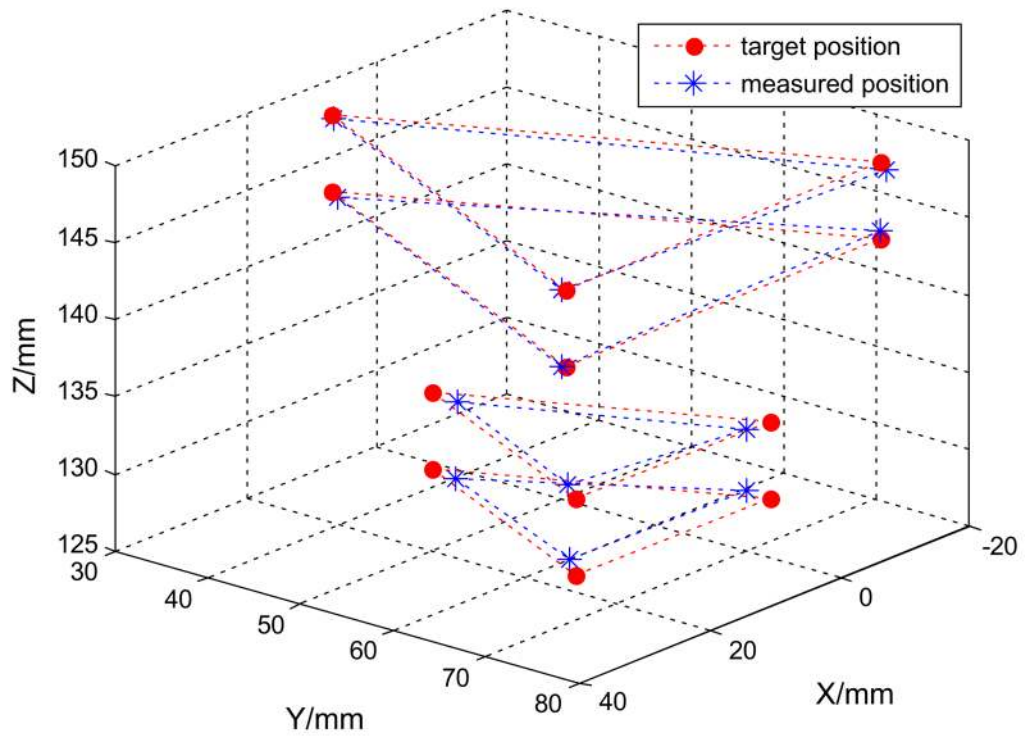
FIGURE 8.
MRI-guided multiple-point targeting results inside a gelatin phantom. The concentric tube robot was closed-loop controlled to move the needle tip to 12 desired points (red circles) in gelatin phantom and the actual position was measured by analyzing acquired MR images (blue stars).
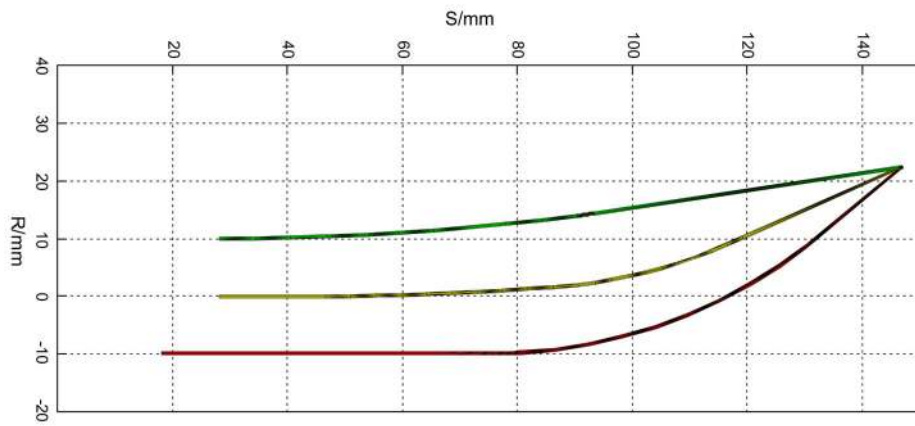
FIGURE 9.
Simulation of the remote center of motion like kinematics of the concentric continuum robot. Three needle placement trajectories reach the same target point, achieved by applying different configurations of both the Cartesian base and the concentric tubes.
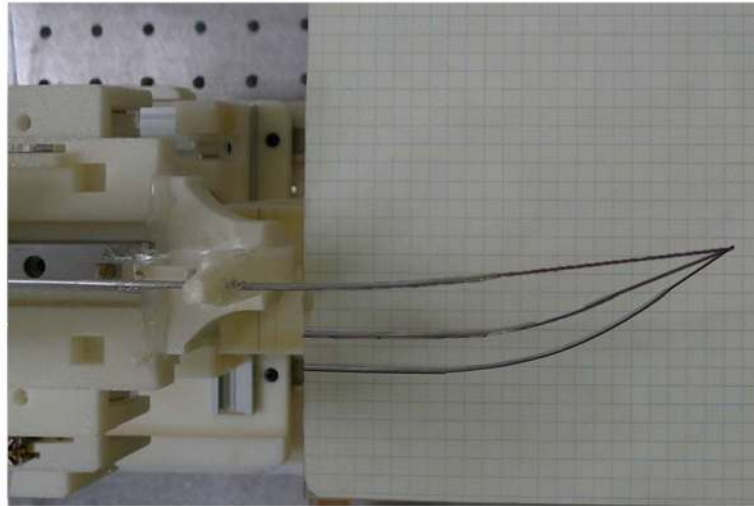
FIGURE 10.
Overlaid camera images of three actual robot trajectories targeting the same point from multiple approach trajectories.

FIGURE 11.
MR images of 3 different concentric tube robot needle insertion trajectories to the same target location in the soft gelatin phantom. Closed-loop inverse kinematics was utilized to reach the same target with different joint space configurations.
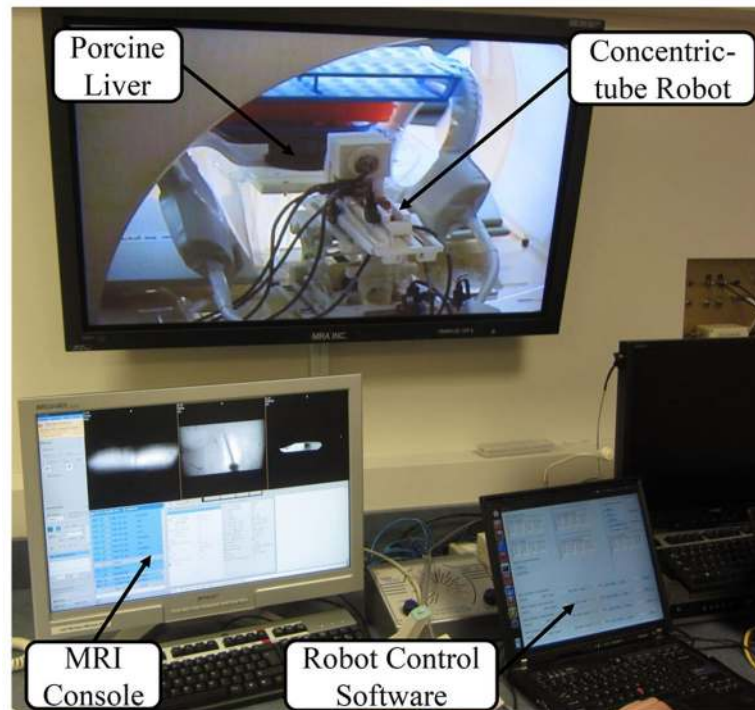
FIGURE 12.
Experimental setup for *ex vivo* tissue evaluation. The interventional robot is inside 3T MRI scanner bore deploying concentric tubes, and the MRI console outside displaying the live MR image of the curved path.
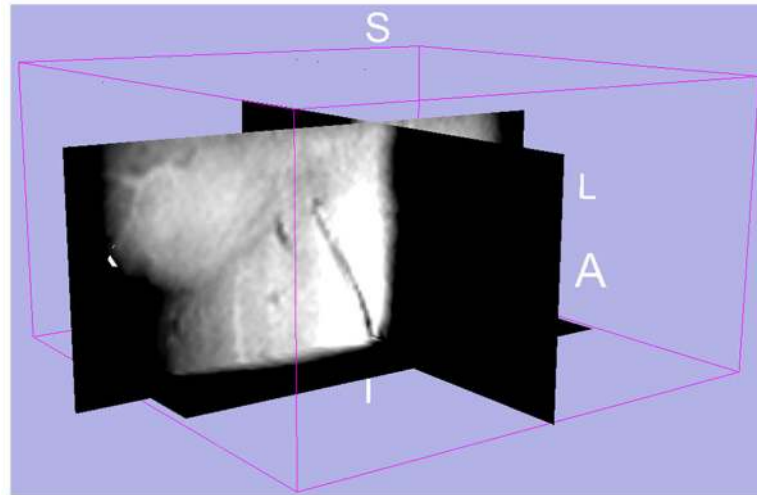
FIGURE 13.
Volumetric MR image showing a representative active cannula path inserted into a *ex vivo* liver by the robot inside the MRI scanner. The cannula is inserted along the I-S direction (vertical in this figure) and is shown in the coronal plane along with additional two cross-sectional planes.
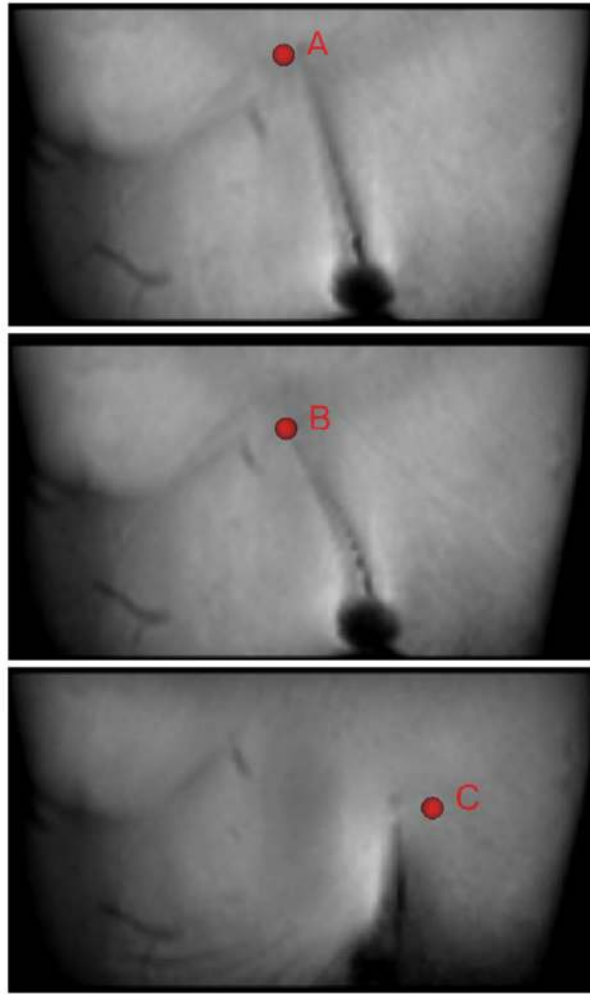
FIGURE 14.
Ex vivo tissue results showing three different selected targets (red spheres) and the corresponding needle trajectory and needle tip location on axial TSE T2 weighted MR images.

TABLE 1

Accuracy assessment of MRI-guided closed-loop needle placement to 3 targets inside an *ex vivo* liver tissue.

No	Target position (mm)			Final tip position (mm)			Error (mm)			Total error (mm)	In-plane(RA) error (mm)
	R	A	S	R	A	S	R	A	S		
1	34.79	63.31	138.17	31.13	63.30	137.19	3.66	0.01	0.98	3.79	3.66
2	3.4.4	63.23	130.00	31.94	63.20	128.04	2.10	0.03	1.96	2.87	2.10
3	2.10	63.10	118.77	7.87	63.14	121.71	−5.77	−0.04	2.94	6.48	5.77
RMS mean							4.13	0.03	2.12	4.64	4.12
Standard deviation							5.05	0.04	2.59	1.87	1.84

Note R, A and S are the coordinates of the needle tip, while RA plane corresponds to axial plane in MRI scanner coordinate system.